

The Growth of Structure I Methane Hydrate from Molecular Dynamics Simulations

Yen-Tien Tung, Li-Jen Chen, Yan-Ping Chen, and Shiang-Tai Lin*

Department of Chemical Engineering, National Taiwan University, Taipei 10617, Taiwan

Received: March 31, 2010; Revised Manuscript Received: June 16, 2010

The key factors that affect the growth of methane hydrates are identified using molecular dynamics simulations. The three-phase molecular models consisting of methane gas, liquid water, and solid hydrate phase are used in this study. The melting temperatures of such a model at different pressures are found to be in good agreement with experiment. The growth rate of methane hydrate is found to be dominated by (1) the solubility of methane in the liquid phase, (2) the diffusivity of methane in water, and (3) the adsorption of methane by methane-filled incomplete water cages at the solid–liquid interface. The solubility, and hence the growth rate, increases with the partial pressure of methane in the vapor phase. The mass transport resistance from adsorption and the diffusion of methane are two competing factors, with the adsorption of methane at the interface found to be the rate-limiting step. The presence of a high concentration of incomplete clathrate hydrate cages presents strong affinity to dissolved methane at temperatures below the melting point. In addition to methane adsorption, water molecules must be expelled to form the complete clathrate cages. Both processes lead to a methane concentration minimum at 5–9 Å in front of the growing interface. The methane concentration minimum provides the driving force for methane transport from the bulk to the interface. There are two types of solid layers of methane hydrate in the (1,0,0) direction. The growths of these layers are different, highly correlated, and affected by the methane concentration. A detailed mechanism of the layer growth is deduced from our simulations.

1. Introduction

Clathrate hydrates are a class of nonstoichiometric crystalline compounds consisting of cavities (or cages) formed by hydrogen-bonded water molecules in which guest molecules are trapped.¹ Methane is one kind of guest molecule that stabilizes the water cages in the clathrate hydrate structure. Naturally occurring methane hydrates are found in the permafrost regions and under the deep sea-floor sediments.^{2,3} The amount of methane entrapped in clathrate is so abundant that it is considered as a potential new source of energy.^{1,4–6} As a consequence, there is growing interest and research activity regarding its recovery^{7–12} and related environmental and ecological impact.^{13–16}

There have been many experiments and field studies conducted to understand the thermodynamics,^{17–22} kinetics,^{23–38} recovery,^{7–12} and transportation^{39–42} aspects of methane hydrate. In addition, molecular dynamics simulations are another powerful tool to investigate the thermophysical, structural, and dynamical properties of methane hydrate^{43–45} and the formation,^{45–59} dissociation,^{60–63} and inhibition^{64–75} mechanisms at the molecular scale.

For example, the nucleation process has been studied by Moon et al.,⁴⁶ Guo et al.,^{47–51} Mastny et al.,⁵² Hawtin et al.,⁵³ and Walsh et al.⁵⁴ It is shown that methane arrangement and the cage-like water clusters are important factors in the nucleation process. In particular, cages filled with the methane molecule present strong affinity to other dissolved methane that facilitates the nucleation process.⁵¹ The growth of methane hydrate has been investigated by Nada,⁵⁵ Vatamanu and Kusalik,⁵⁶ and English and MacElroy.⁵⁹ A two-step growth process was suggested that involves methane molecules occupying the cage sites, followed by the reordering of water

molecules (to form the cages). Interesting structure transition from sI to sII^{56,57} was reported and a new structure, structure K, is found to be a factor leading to this transition.

The structure and properties of the solid–liquid interface was found to play an important role in the growth of methane hydrates. Vatamanu and Kusalik⁵⁶ reported that the interface has a strong affinity to methane molecules during the growth process. Nada⁵⁵ showed that as the methane molecules approaches the interface, the surrounding water molecules are sandwiched, which helps the formation of water cages. Although these studies explain the process of the growth of methane hydrate, the active transport of methane molecules against concentration gradient (i.e., from low concentration in the bulk to high concentration at the interface) was not addressed. Furthermore, Nada⁵⁵ reported an increased growth rate at high initial methane concentrations. In the steady-state simulation of Vatamanu and Kusalik,⁵⁸ no clear temperature or pressure dependence of the growth rate was observed. However, qualitative and semiquantitative relations among the growth factors (growth rate, interface properties, methane solubility, temperature, pressure, etc.) are still lacking.

One purpose of this work is to address these issues and to provide a clearer picture on the growth of methane hydrates upon changing of growth conditions. The growth of methane hydrates below the melting point is investigated over a wide range of pressures. Varying the system pressure allows for a significant change in the growth conditions, thus providing fruitful data for understanding the growth mechanism. The solubility of methane, its distribution across the solid–liquid interface, and development of water cages at the interface are analyzed. These are found to be the key factors that determine the growth rate of methane hydrates and can be considered in a simple adsorption-diffusion model. A detailed mechanism that

* To whom correspondence should be addressed. E-mail: stlin@ntu.edu.tw.

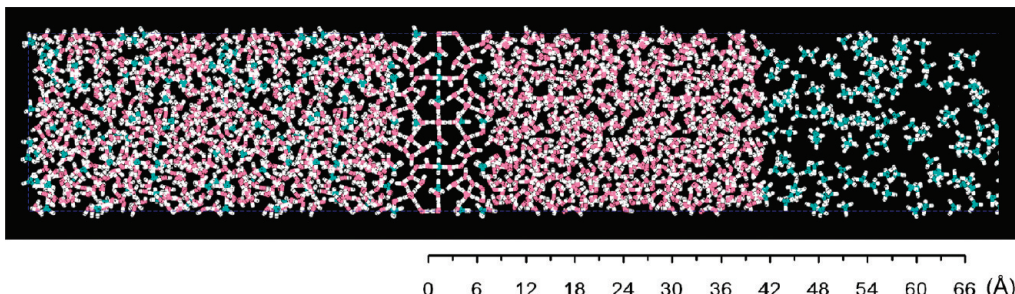


Figure 1. The initial molecular structure of a three-phase methane hydrate model. This model consists of a $1 \times 2 \times 2$ structure I hydrate slab (in the middle), two liquid slabs (pure water on the right-hand side, and one methane–water mixture on the left-hand side), and a vapor slab (mostly methane). Carbon atoms are shown in green, oxygen in red, and hydrogen in white. The scale bar shown below the figure indicates the size of the model.

TABLE 1: The Parameters for Lennard-Jones 12-6 Potential and Atomic Charges Used in This Work

element	molecule	ϵ (kcal/mol)	σ (Å)	charge
O	H ₂ O	0.163	3.164	
H		0.000	0.000	0.5242
M				-1.0484
C	CH ₄	0.066	3.500	-0.2400
H		0.030	2.500	0.0600

involves the transport of both methane and water molecules is derived from the results of our simulations.

2. Computational Details

The three-phase model, as shown in Figure 1 and consisting of a methane gas, a liquid water, and a solid hydrate phase, is used in this study. The methane gas phase contains 160 methane molecules, and the hydrate phase consists of a $1 \times 2 \times 2$ unit cell of structure I (sI) crystalline hydrate with all its cavities (both inside and at the surface) filled with methane (i.e., 184 water molecules and 44 methane molecules). [Note that the sI unit cell contains 46 water molecules, 6 large $5^{12}6^2$ cavities, and 2 small 5^{12} cavities.] The crystalline hydrate is created following the Bernal–Fowler ice rules.⁷⁶ Two liquid slabs are placed between the gas and solid phases: one pure liquid water slab (736 water molecules, on the RHS of the solid phase in Figure 1) and one liquid water slab supersaturated with methane (736 water and 128 methane molecules, on the LHS of the solid phase in Figure 1). Note that the methane concentration in the latter water slab is the same as that of sI methane hydrate, which is above the methane solubility in water in our study. The introduction of two liquid slabs in our model allows for the study of the concentration effect on the growth rate of methane hydrate. The high methane concentration slab may also serve as a buffer region for methane in the dynamic simulations. The size of such an initially created model (using molecular simulation package Cerius²)⁷⁷ is $135.00 \text{ \AA} \times 23.74 \text{ \AA} \times 23.74 \text{ \AA}$.

The TIP4P-Ew⁷⁸ (for water) and OPLS-AA⁷⁹ (for methane) force field is chosen to describe the interactions within the molecular model. The TIP4P force field has been used to study gas hydrate systems.^{44,56,58,74,80–82} The atomic charge and Lennard-Jones interaction ($V(r) = 4\epsilon[(\sigma/r)^{12} - (\sigma/r)^6]$) parameters are summarized in Table 1. The geometric combination rule ($\epsilon_{ij} = (\epsilon_i\epsilon_j)^{1/2}$ and $\sigma_{ij} = (\sigma_i\sigma_j)^{1/2}$) is used for the LJ parameters between different types of atoms, except that $\sigma = 3.032 \text{ \AA}$ and $\epsilon = 0.255 \text{ kcal/mol}$ (obtained by fitting to the QM calculated interactions by Cao et al.^{83,84}) are used for O (of water) and C (of methane) interactions. The methane–water potential of Cao et al. was developed specifically for TIP4P-Ew water and OPLS-

AA methane and has been shown to give good occupancy numbers of methane hydrates.

All the subsequent molecular mechanic and dynamic simulations are performed using the open source package, LAMMPS.⁸⁵ The initially created model is first energy-minimized and a short, 20 ps, NVT simulation at 200 K is performed to relax any extra stress at the solid–liquid and the liquid–gas interfaces. The relaxed system is then heated from 200 to 260 K at a rate of 0.5 K/ps under constant pressure. Finally, the system is subjected to long (40 ns at 30, 60, 100 MPa, and 60 ns at 10 MPa) NPT simulations for the study of methane hydrate growth.

The pressure effect is studied by using four sets of simulations at pressures of 10, 30, 60, and 100 MPa, respectively. The statistical uncertainties are assessed by performing three independent sets of simulations (using a different random seed for velocity initialization) at each pressure–temperature condition. The periodic boundary condition is applied to the simulation box in all three directions. The Nose–Hoover temperature thermostat⁸⁶ with a relaxation time of 0.1 ps and pressure barostat⁸⁷ with the relation time of 1 ps are used.⁸⁸ The integration time step is set to 1 fs. In our NPT simulations, two independent barostats with the same target pressure are used, one for the normal stress in the x direction (the growth direction, see Figure 1) and the second for the y and z directions. The Lennard-Jones potential energy is calculated with a cutoff of 9.5 \AA (around three times σ of the O atom), and the long-range Coulomb energy is calculated by PPPM^{89–91} with a cutoff of 8.5 \AA for the real part calculation.

The three-phase (hydrate, liquid, and vapor, H–L–V) coexisting equilibrium temperatures of methane hydrate at the four studied pressures are determined by performing a series of simulations at several temperatures around the melting temperature for each pressure of interest. The initial structure for such simulations is taken from an NPT simulation at 30 MPa and 260 K after 20 ns, as shown in Figure 2, where the solid hydrate phase is grown to a thickness of 47 \AA (about $4 \times 2 \times 2$ (sI) crystalline hydrates). The size of the initial structure is around $129.2 \text{ \AA} \times 23.6 \text{ \AA} \times 23.6 \text{ \AA}$. All simulation parameters are the same as those used for the growth study described previously. At a desired pressure, the temperature of the initial structure is increased to the desired one from 260 K at a rate of 0.5 K/ps. Subsequent NPT simulations are performed for up to 20 ns, and the thickness of the solid hydrate phase is examined. The simulations performed are summarized in Table 2.

The angular order parameter (AOP) of a water molecule is an index to identify the structural characteristic of water configuration and is defined as

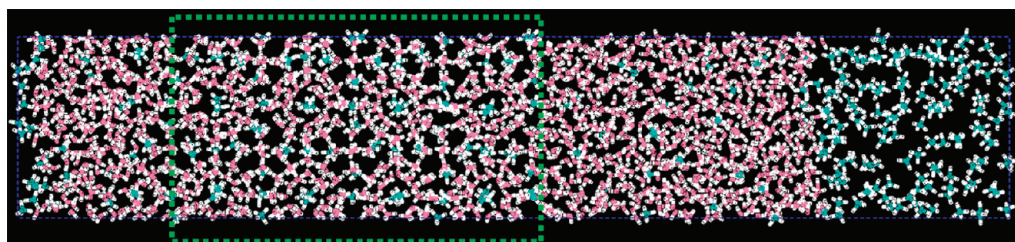


Figure 2. The initial structure used in the measurement of three-phase equilibrium temperatures. The solid phase is emphasized in the rectangular area of green dashed lines.

TABLE 2: The Three Phase (hydrate-liquid-vapor) Coexisting Temperature T_m and Pressure P Determined from Molecular Dynamics Simulations

P (MPa)	T_m from MD (K)	T_m from Experiment (K)	simulated temps (K) (simulation time ns)
10	281 ± 3	285 (8.66 MPa)	275 (10), 280 (10), 283 (10), 285 (10), 290 (10), 296 (10), 301 (10)
30	289 ± 3	295 (30.35 MPa)	285 (20), 288 (10), 290 (20), 293 (10), 295 (10), 301 (10)
60	295 ± 2	300 (56.70 MPa)	288 (10), 290 (10), 293 (20), 295 (10), 298 (20)
100	299 ± 3	305 (96.43 MPa)	295 (20), 298 (20), 300 (20), 304 (10), 309 (8)

$$\text{AOP} = \sum [(\cos \theta |\cos \theta) + \cos^2(109.47^\circ)] \quad (1)$$

where θ is the inclusion angle among the oxygen atom of the water molecule of interest and any two oxygen atoms of the neighboring water molecules. The summation runs over all possible θ of water molecules within a radius of 3.5 Å from the center oxygen atom of interest. The angular order parameter is widely used to identify hydrate-like water molecules^{53,59,60,62} in gas hydrate simulations and the structure of water cluster in solvation systems.⁹² The average AOP of ice and hydrate crystalline structure are 0⁹³ and 0.1, respectively, whereas that of liquid water (amorphous) is about 0.8. The interface between the solid hydrate and the liquid can thus be conveniently defined as the location where the AOP of water is 0.4, as shown in Figure 3. The growth rate of hydrate is determined from the rate of the interface movement. All our simulation temperatures are above the ice melting point of TIP4P-Ew water (around 245 K^{94–96}), and no ice structure was found in our simulations.

The AOP of water molecules is also used to identify three types of water cages (or cavities) that may enclose a methane molecule: large ($5^{12}6^2$) cage, small (5^{12}) cage, and partial (or incomplete) cage. Three variables are determined for each of the methane molecules in the liquid and solid phase: (1) the number, n_w , of water molecules within radius of 5.5 Å from the carbon atom of the methane molecule; (2) the number, n_h , of hydrate-like water molecules (AOP < 0.4) (out of the n_w molecules); and (3) the number, n_b , of hydrogen bonds formed from these hydrate-like water molecules, n_b . For an ideal complete large cage, $n_w = n_h = 24$ and $n_b = 36$, whereas for an ideal complete small cage, $n_w = n_h = 20$ and $n_b = 30$. If $13 \geq n_h \geq 10$, the methane molecule is enclosed in a half-complete (partial/incomplete) cage. In the case of $n_h \geq 14$, a half-complete (partial/incomplete) cage is identified if it is not an irregular large or small cage.⁶²

3. Results and Discussion

3.1. Equilibrium Phase Diagram. The Gibbs degrees of freedom of a three-phase (H–L–V) methane–water system is unity ($F = C + 2 - P = 2 + 2 - 3 = 1$), meaning that at a given pressure, such a system is stable only at the correct melting temperature, and the solid hydrate phase may either grow or melt if the temperature is below or above this temperature. Figure 4a shows the changes in the thickness of the solid phase with time at different temperatures (295, 298, 300, 304, and

309 K) and 100 MPa. It can be seen that the amount of methane hydrate fluctuates at 298 and 300 K, increases at 295 K, and decreases above 304 K. The melting/crystallization of the solid hydrate phase is also evidenced by the change in the potential energy of the system, as shown in Figure 4b. The increase in potential energy (PE) at 304 K indicates melting,⁹⁵ whereas the decrease in PE at 295 K indicates crystallization. At 298 and 300 K, the PE of the system fluctuates around -11.5 kcal/mol (note that the energy is normalized to 1 mol of water molecules). On the basis of these observations, we conclude that the three-phase equilibrium temperature at 100 MPa is around 299 K.

Repeating such simulations and analysis at other pressures (60, 30, and 10 MPa) gives the melting temperature as a function

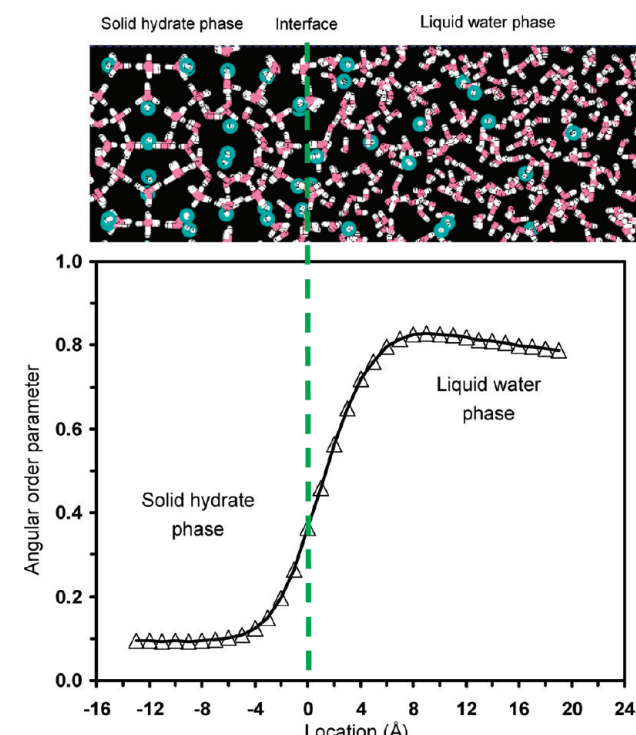


Figure 3. The typical distribution (obtained from the system of methane hydrate at 30 MPa and 260 K) of the angular order parameter of water molecules in the direction perpendicular to the solid–liquid interface. The solid–liquid interface (green dashed-line) is defined at $\text{AOP} = 0.4$.

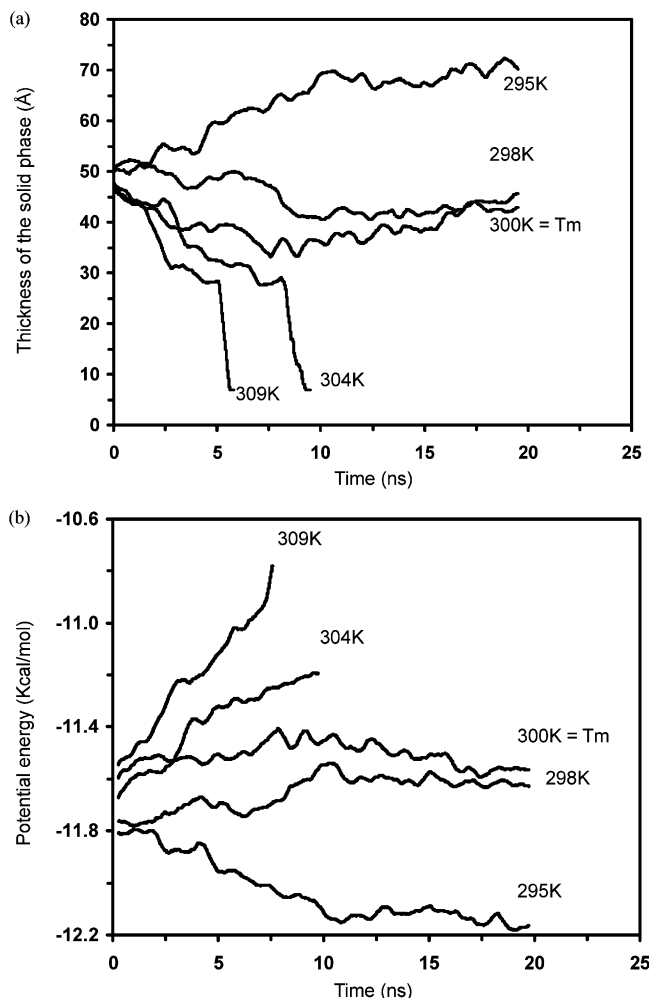


Figure 4. The change in the thickness of the solid phase (a) and the potential energy (normalized to 1 mol of water molecules) (b) with time at 100 MPa and different temperatures (295, 298, 300, 304, and 309 K).

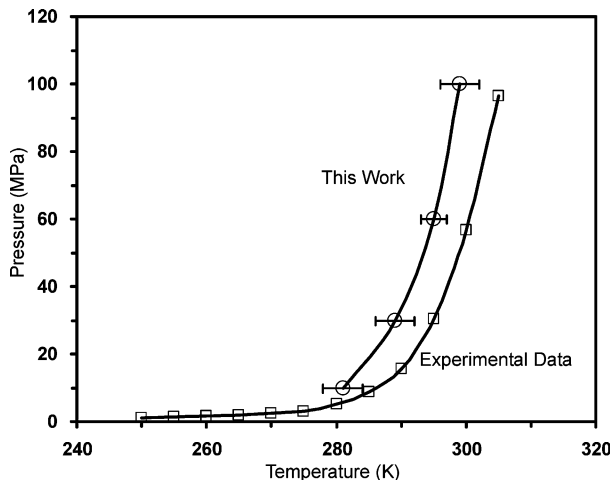


Figure 5. The comparison of the melting temperatures from MD simulations (○) and experimental results (□).

of pressure, as summarized in Table 2 and shown in Figure 5 (note in Table 2 that the value of 299 for the case of 100 MPa is the average of 298 and 300 K, and the uncertainty is estimated from the temperature difference between 298 and 295 K. Similar estimates are used to estimate the average and uncertainty at other pressures). As can be seen in Figure 5, the melting temperatures from simulation are consistently lower than the

experimental values by about 5 K at all pressures. Nonetheless, the melting curve is in good agreement with experimental data^{17–19} (open squares). These results support that the model and force field used in this study are adequate for the study of the methane hydrate growth.

3.2. Growth Rate of Methane Hydrate. NPT simulations at 260 K and four pressures were conducted to study the growth of methane hydrate. From Figure 5, the temperature of 260 K is well within the hydrate stability region. Figure 6 illustrates the snapshots of NPT simulations at 60 MPa and 260 K. It can be seen that the solid phase increases significantly over a time span of 40 ns. By using the AOP as an index for identifying the location of solid–liquid interface, the increase of thickness of the solid phase with time can be quantified, as shown in Figure 7. (Note that the 0 ns in Figure 7 is the beginning of the production simulation, at which point the system has undergone the equilibration process of energy minimization and a short, ~240 ps, NVT and NPT simulation. Therefore, methane molecules have already entered the liquid phase.) The slope of such curves indicates the rate of the linear growth of the clathrate hydrate. It can be seen that the growth rate is nearly constant over the time span of our simulation. Furthermore, the growth rate increases with the pressure of the system, from 0.4 Å/ns at 10 MPa to 1.1 Å/ns at 100 MPa. The growth rates observed in our simulations are similar to that found by Vatamanu and Kusalik⁵⁶ (1.0–1.5 Å/ns at 264–263 K) and Nada⁵⁵ (~0.54 Å/ns at 100 MPa and 298 K).

To better understand the reason why high pressure enhances the growth rate of methane hydrate, the methane concentration in the liquid water at these four pressures is examined. Figure 8 shows the average methane concentration in the liquid water during the growth simulations. The average methane concentration increases with pressure and is in positive correlation with the growth rate of solid hydrate. Therefore, high solubility of methane at high pressures facilitates the solidification process. Note that at low pressures (10 and 30 MPa), the concentration of methane may stay nearly constant over a long period of time (quasi-steady state), but at high pressures (60 and 100 MPa), the methane concentration may increase rapidly near the end of simulation. This is because the liquid slab becomes very thin near the end of high pressure simulations, and the dissolution of gaseous methane may become very rapid. Separately, the initial growth rates (first simulation period of 5 ns) in the liquid water initially supersaturated with methane (0.17 methane molecules per water molecule; i.e., the same methane concentration as that in the solid phase) is found to be very high, around 3.63 Å/ns, and not to be pressure-dependent. This provides strong evidence that the methane concentration in the liquid phase is an essential factor to the growth rate of methane hydrate.

The distribution of the methane concentration along the direction perpendicular to the solid–liquid interface also provides insights into the mechanism of the hydrate growth. Figure 9 illustrates such a distribution from the simulations at four different system pressures. The origin of the x-axis indicates the location of the solid–liquid interface. The negative and positive locations indicate the region in the hydrate (where methane concentration approaches 0.17 CH₄ per water) and the liquid water regions (where methane concentration approaches the bulk phase concentration as shown in Figure 8), respectively. Each distribution is averaged over the period where the solid phase thickness increases from 12 to 24 Å (i.e., during the period when the growth rate is almost constant as shown in Figure 7; the thickness of the liquid water region at the end of the analysis

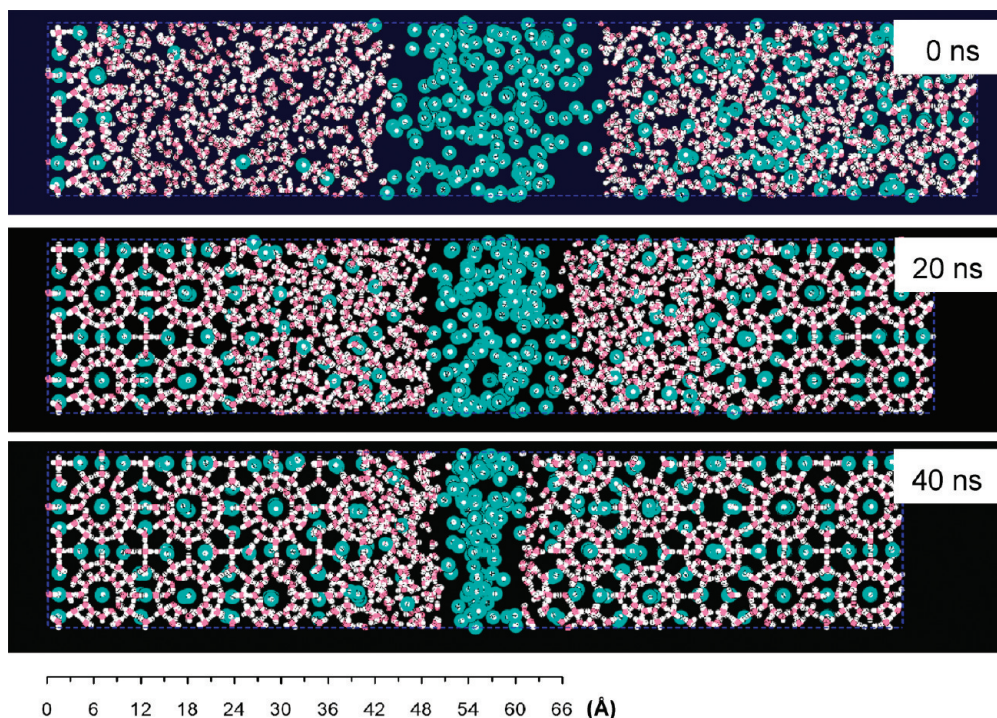


Figure 6. Snapshots taken from the methane hydrate growth simulation at 60 MPa and 260 K.

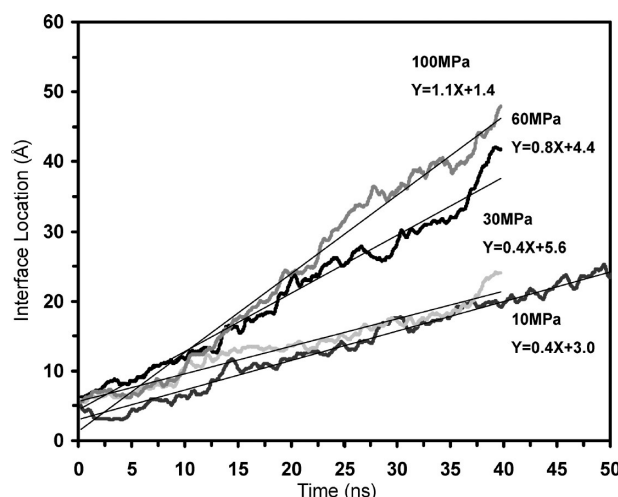


Figure 7. The time evolution of the solid–liquid interface from NPT simulations at 260 K and 4 pressures (10, 30, 60, and 100 MPa). The slope of these curves indicates the growth rate of methane hydrate.

period is still greater than 20 Å). A common feature in the methane distributions is that there exists a concentration minimum at 5–9 Å in front of the interface. This region is referred to as the methane depletion zone (MDZ). The presence of a MDZ implies that the methane is rapidly absorbed at the solid–liquid interface during the growth of hydrate. It is interesting to note that the interfacial widths are assessed as the range of 10–12 Å from the analysis of the potential energy profile by Vatamanu and Kusalik,⁵⁶ which encompasses the MDZ observed here.

The rapid uptake of methane at the solid–liquid interface, or the growing layer, is considered driven by the high level of methane-filled half-complete water cages. Figure 10 shows the concentration distribution of incomplete cages across the solid–liquid interface at different pressures (10, 30, 60, and 100 MPa). It is quite clear that the concentration of incomplete cages peaks right at the interface and quickly decreases in the

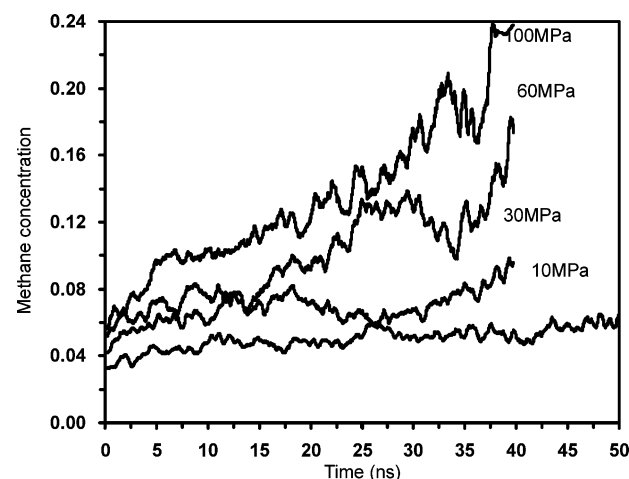


Figure 8. The average concentration of methane in the liquid phase at 260 K and four pressures (10, 30, 60, and 100 MPa).

bulk liquid and solid phases. Guo et al.⁵¹ showed that the potential of mean force (PMF) between methane molecules that are partly enclosed by cage-like water clusters are significantly stronger than the PMF between two bare methane molecules. In other words, these incomplete water cages present strong affinity to the methane molecules at temperatures below the melting point, allowing methane molecules to be transported to a higher concentration region (note that the methane concentration is highest in the solid phase). The attraction of dissolved methane to such incomplete water cages is consistent with the recent observation of Guo.⁵¹

On the basis of these observations, the growth of methane hydrate can be modeled using a simple adsorption–diffusion model. The mass flux of methane from the bulk to the MDZ is driven by the concentration differences in the bulk (C_{bulk}) and the minimum concentration in the MDZ (C_{min}) as

$$\text{rate} = h(C_{\text{bulk}} - C_{\text{min}}) \quad (2)$$

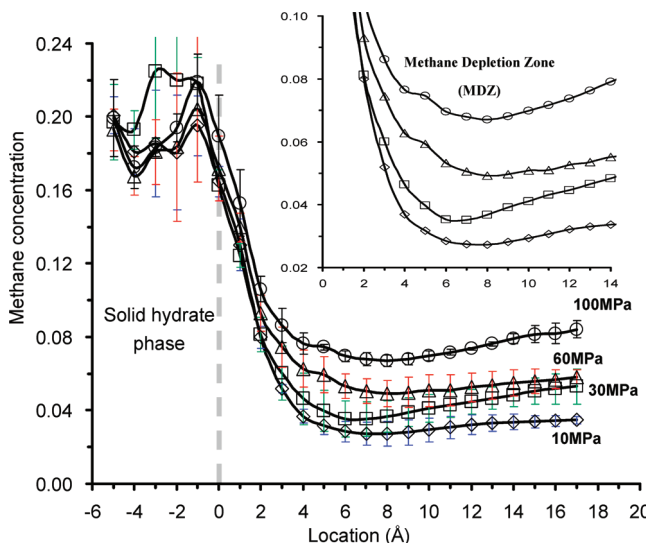


Figure 9. The distributions of methane concentration along the direction perpendicular to the solid–liquid interface (origin of x -axis) at 10 (\diamond), 30 (\square), 60 (\triangle), and 100 (\circ) MPa across the surface of growing methane hydrate. The inset figure emphasizes the concentration variation near the methane concentration minimum. The average and standard deviations are estimated from three sets of independent simulations.

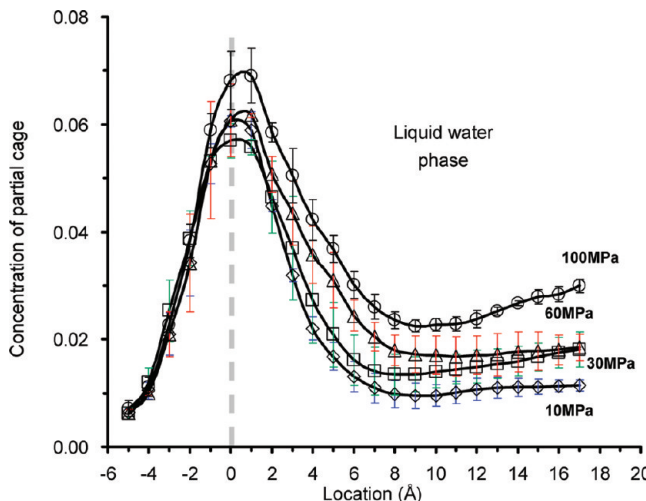


Figure 10. The concentration distribution of methane-filled incomplete cages along the direction perpendicular to the solid–liquid interface at 10 (\diamond), 30 (\square), 60 (\triangle), and 100 (\circ) MPa. The average and standard deviations are estimated from three sets of independent simulations.

where h is a mass transfer coefficient. The adsorption of methane in the growing layer (between the interface and the MDZ) is considered as a first-order reaction

$$\text{rate} = kC_{\min} \quad (3)$$

where k is a rate constant. At steady state, the two rates (eq 2 and 3) are the same, and we may obtain the minimum methane concentration as

$$C_{\min} = \frac{C_{\text{bulk}}}{1 + k/h} \quad (4)$$

Therefore, the ratio of k/h determines minimum methane concentration in the MDZ. A very small value of C_{\min} can be

observed in the case when $h \ll k$. The value of C_{bulk} is estimated from the methane concentration at the location of 17 Å away from the interface (see Figure 9). Table 3 summarizes the values of k/h determined from our simulations. The ratio k/h decreases from 0.4 at 10 MPa to 0.25 at 100 MPa. The growth rate can now be associated with the bulk phase concentration,

$$\text{rate} = \frac{C_{\text{bulk}}}{1/k + 1/h} \quad (5)$$

From eq 5, we see that the growth rate of methane hydrate is dominated by three factors: (1) the bulk phase methane concentration, (2) the mass transport of methane in the bulk phase, and (3) the methane adsorption by water cages in the growing layer. The methane concentration in the bulk water phase increases with the increase of partial pressure of methane in the vapor phase. Therefore, increasing pressure always leads to an enhancement of growth rate. The diffusion (h) and adsorption (k) of methane present as the competing mass transport resistance to the growth of methane hydrate. At the melting point, there is no driving force for methane adsorption by the partial water cages ($k = 0$), and the growth of hydrates ceases. The fact that the k/h is slightly less than unity (see Table 3) indicates that the growth process at 260 K is still limited by the methane uptake at the interface. It is noteworthy that the mass transport of methane was found to be the limiting step⁶¹ in the melting process.

It is useful to make note of the occupancy fraction of methane in the hydrate cavities. Although the cavities in the initial $1 \times 2 \times 2$ hydrate crystal are 100% occupied by methane, our analysis shows that the occupancy of subsequently grown layers does depend on the pressure. The occupancy of large cavities in the subsequently formed hydrate at 10, 30, 60, and 100 MPa are $80.6 \pm 4.8\%$, $81.9 \pm 2.4\%$, $81.9 \pm 2.4\%$, and $86.1 \pm 4.8\%$, respectively; whereas these numbers are $91.7 \pm 14.4\%$, $83.3 \pm 14.4\%$, $70.8 \pm 19.1\%$, and $87.5 \pm 12.5\%$, respectively, in the case of small cages.

3.3. Methane and water Transport. There are two types of layers in the structure I clathrate hydrate in the $(1, 0, 0)$, $(0, 1, 0)$ or $(0, 0, 1)$ direction: one containing 36 water molecules and 12 methane filled cavities (type I), and the other containing 56 water molecules and 4 methane filled cavities (type II). Both layers are ~ 3 Å thick, as depicted in Figure 11. Figure 12a shows the evolution of methane-filled cage, water, and methane molecules, in layer 5 (type I) of growing methane hydrate at 30 MPa and 260 K. Methane molecules are attracted into layer 5 at 9 ns (beginning of the growth), and the growth is completed at 35 ns with the number of methane molecules increased to 11 (one cage is unoccupied). Because a significant amount of methane molecules are attracted into the type I layer, expulsion of water molecules begins to proceed. The number of water molecules decreases from 56 to 36, and the originally hydrophilic layer changes to being more hydrophobic one (fewer water and more CH_4 molecules), which is beneficial to cage organization. We also observed a similar entering of methane and expulsion of water molecules at other pressures in the growth of type I layers. The ratio of methane to water molecules increases when the entering of methane molecules and expulsion of water molecules proceeds. Finally, the ratio of methane to water molecules increases with time to a value of around 0.33 (this value depends on the cage occupancy), which is the methane composition of hydrate in the type I layer.

Figure 12b shows the evolution of methane-filled cage, water, and methane molecules in layer 6 (type II) of growing methane

TABLE 3: The Conditions and Simulation Time Used in the Simulations for the Growth of Methane Hydrate^a

P (MPa)	simulation time (ns)	T (K)	growth rates (Å/ns)	C_{\min} (CH ₄ per H ₂ O)	C_{bulk} (CH ₄ per H ₂ O)	k/h
10	60	260	0.38 (0.10)	0.027 (0.006)	0.035 (0.002)	0.38 (0.19)
30	40		0.49 (0.09)	0.035 (0.009)	0.053 (0.010)	0.55 (0.16)
60	40	260	0.89 (0.05)	0.049 (0.007)	0.058 (0.004)	0.20 (0.13)
100	40	260	1.05 (0.07)	0.067 (0.003)	0.084 (0.005)	0.25 (0.01)

^a The average numbers and standard deviations (in the parentheses) are obtained from three sets of independent simulations at the same P/T conditions.

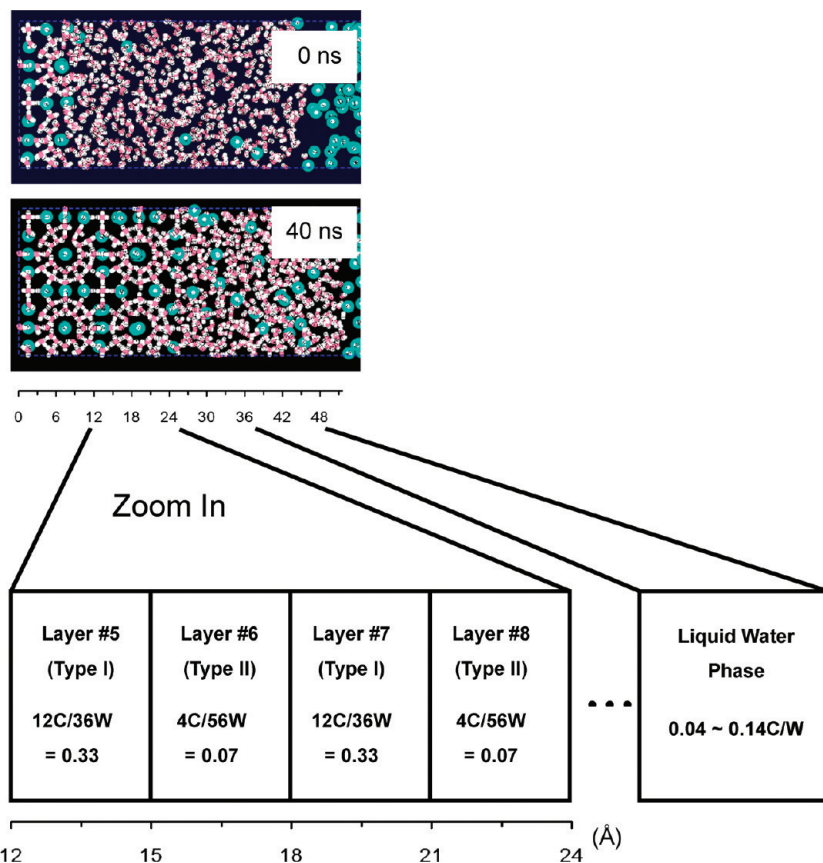


Figure 11. Illustration of arrangement of hydrate layers and the assigned identification number used in this work.

hydrate at 30 MPa and 260 K. The methane-filled cage formation begins at 20 ns, continues, and is completed at \sim 38 ns. Unlike the situation in type I layers, the evolution of the number of water molecules in the type II layer is different. The number of water molecules increases from 50 to 56, since during the growth of its previous type I neighbor, 20 water molecules (56–36) are expelled and enter this growing type II layer. The needed 6 water molecules are thus supplied from its previous neighboring layer. It is interesting to note that the methane concentration in layer 6 decreases to zero at 18 ns (depletion of methane). During this period, the cage formation in layer 5 pauses (16–20 ns, Figure 12a). Therefore, the growths of these two types of layers are highly correlated.

Figure 13 shows the time evolution of methane-filled cage numbers in layers 5–8 at all four pressures. It can be seen that the type II layer (e.g., layer 6) starts to grow when its previous type I layer (e.g., layer 5) reaches about 25–50% of its completion. Furthermore, the growth of a type II layer (e.g., layer 6) also initiates the growth of its next adjacent type I neighbor (e.g., layer 7). The growth of type II layers (e.g., layer 6) is completed at about the same time as its previous type I neighbor (e.g., layer 5). Therefore, the rate of cage formation

in a type II layer is slightly faster than that in a type I layer due to the reduced methane demand for cage formation in the type II layer.

From the perspective of the growth of layers of the same type, it is found that a type I layer (e.g., layer 7) may start to grow when its previous type I layer (e.g., layer 5) reaches \sim 50% of its completion. However, a type II layer (e.g., layer 8) starts to grow only when its previous type II layer (e.g., layer 6) is nearly complete. This provides more strong evidence for the correlation in the growth of the two types of layers. Figure 14 illustrates such a correlation using the pentagonal rings^{97–100} (green line) identified using the hydrogen bonded water molecules. Perfect sI clathrate hydrates consist of pentagonal and hexagonal rings^{45,49,50} (e.g., large cages are $5^{12}6^2$ and small cages are 5^{12}). The snapshots taken are nearly at the beginning of the growth of the layers 5, 6, 7, and 8 at 30 MPa and 260 K. It can be seen that the pentagonal structures in layers 5 and 6 do not complete until the start of growth the layer 8. In addition, the pentagonal structures start to appear in layers 6 and 7 before the completion of layer 5.

3.4. Growth Mechanism of Methane Hydrate. On the basis of the results of our simulations, we may summarize the growth mechanism of methane hydrate as follows:

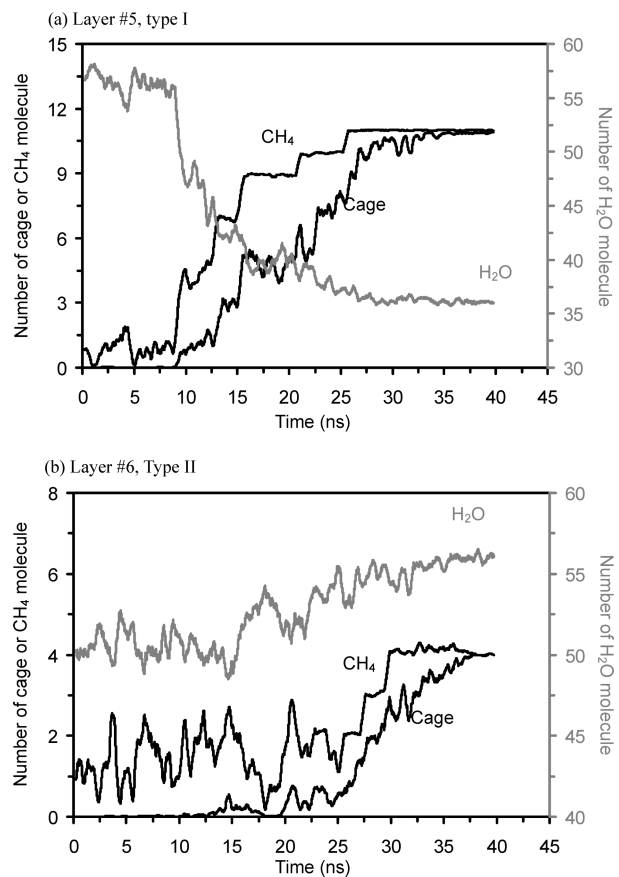


Figure 12. The time evolution of methane-filled cage, methane, and water molecules at 30 MPa and 260 K in layer 5 (type I) (a) and layer 6 (type II) (b) of a growing methane hydrate layer.

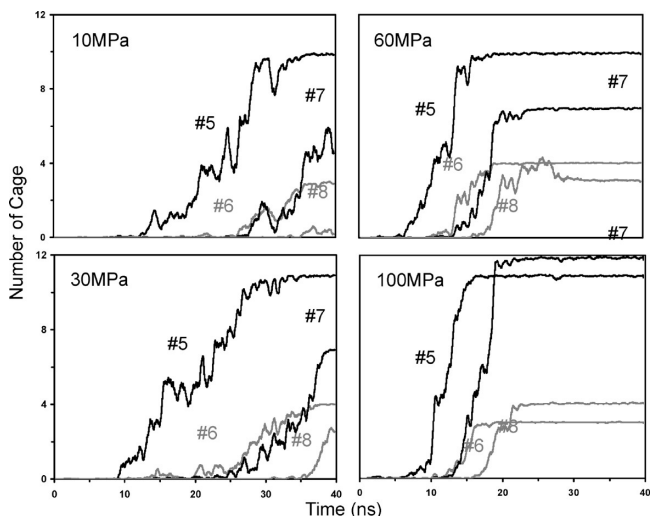


Figure 13. Time evolution of methane-filled cages in layers 5–8 (as defined in Figure 11) at 260 K and four pressures.

1. Cagelike water clusters attracts methane molecules to the solid–liquid interface. The affinity of the methane molecules to the incomplete water cages increases with the deviation of temperature from the melting point.

2. The attraction of methane molecules to the methane-filled incomplete cages (and the expulsion of water molecules that is stated next) leads to a minimum methane concentration at $\sim 5\text{--}9\text{ \AA}$ in front of the interface. The minimum methane concentration provides the driving force (concentration gradient) for methane transport from the bulk to the interface.

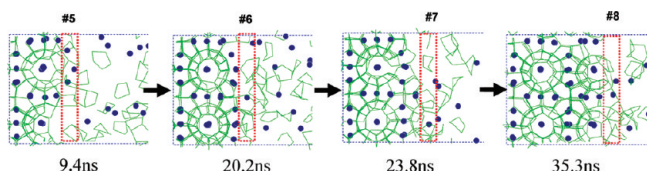


Figure 14. The development of pentagonal structures (indicated by the green lines) at the beginning of growth of layers 5 (9.4 ns), 6 (20.2 ns), 7 (23.8 ns), and 8 (35.3 ns) at 30 MPa and 260 K.

3. The transport of methane molecules to the interface is accompanied by the expulsion of water molecules. The growth of type I layer requires input of 12 CH₄ molecules and expulsion of ~ 20 (56–36) water molecules. The growth of a type II layer requires a supply of four CH₄ and about six (50–56) water molecules. Overall, the growth of SI hydrate layers would require constant expelling of about 14 (20–6) water molecules.

4. The growth of a type I layer starts with its previous adjacent type II layer and is complete at about the same time as its next adjacent type II layer. The growth of a type II layer starts when its previous adjacent type I layer is half complete and is complete at about the same time as its previous adjacent type I layer. The growth of a type II layer also initiates the growth of its next adjacent type I layer.

4. Conclusions

We studied the pressure effect on the growth rate of methane hydrate at 260 K by molecular dynamics simulation. It is found that the growth rate of methane hydrate is dominated by three key factors: the methane solubility in the water phase, the mass transport of methane by diffusion, and the affinity of methane to incomplete water cages at the interface. The solubility of methane increases with its partial pressures in the vapor phase, resulting in an increased growth rate at high pressures. High concentrations of methane-filled incomplete water cages are found at the solid–liquid interface. At a temperature lower than the melting point, these incomplete water cages provide a strong affinity to methane in solution. As methane molecules are absorbed to the interface, water molecules are expelled to form the (lower density) clathrate hydrate cages. As a consequence, the methane concentration comes to a minimum about $5\text{--}9\text{ \AA}$ in front of the interface. Therefore, the growth rate is determined by the competition of methane adsorption at the interface and the methane diffusion from the bulk to the interface. At the melting point, the affinity of methane to the interface becomes zero, and the solidification ceases.

On a molecular scale, the growth of the methane hydrate is affected by the structure of SI crystal. Two distinct types of layers can be identified by the amount of methane content: type I consists of 12 methane and 36 water molecules, and type II consists of 4 methane and 56 water molecules. In addition to the supply of methane during the growth of methane hydrate, a large amount of water molecules is expelled (reducing the content from 56 to 36) during the growth of type I layers and a small amount is used (increasing from 50 to 56) during the growth of type II layers. Overall, 14×2 water molecules are expelled during the growth of a $1 \times 2 \times 2$ unit structure. The growth of type II layers begins when this previous adjacent type I layer is half completed, and its growth also initiates the growth of its next adjacent type I layer. The methane concentration in the adjacent layers (methane depletion zone) may have significance in the dynamic growth of methane hydrates.

Acknowledgment. The authors thank Professor Jeffery B. Klauda at the University of Maryland for providing us the force

field parameters and many fruitful discussions. Financial support from Grants 97-5226903000-02-04 and 98-5226904000-04-04 from the Ministry of Economic Affairs of Taiwan, NSC 97-2221-E-002-085 and NSC 98-2221-E-002-087-MY3 by the National Science Council of Taiwan, and computation resources from the National Center for High-Performance Computing of Taiwan and Computer and Information Networking Center of National Taiwan University are acknowledged.

References and Notes

- (1) Sloan, E. D.; Carolyn, A. K. *Clathrate Hydrates of Natural Gases*, 3rd ed.; CRC Press: London, 2008.
- (2) Kvenvolden, K. A. *Proc. Natl. Acad. Sci. U.S.A.* **1999**, *96*, 3420.
- (3) Collett, T. S. *AAPG Bull.* **2002**, *86*, 1971.
- (4) Klauda, J. B.; Sandler, S. I. *Mar. Petrol. Geol.* **2003**, *20*, 459.
- (5) Klauda, J. B.; Sandler, S. I. *Energy Fuels* **2005**, *19*, 459.
- (6) Holder, G. D.; Kamath, V. A.; Godbole, S. P. *Annu. Rev. Energy* **1984**, *9*, 427.
- (7) Kang, S. P.; Lee, J. W.; Ryu, H. J. *Fluid Phase Equilib.* **2008**, *274*, 68.
- (8) Li, X. S.; Wan, L. H.; Li, G.; Li, Q. P.; Chen, Z. Y.; Yan, K. F. *Ind. Eng. Chem. Res.* **2008**, *47*, 9696.
- (9) Shin, K.; Park, Y.; Cha, M. J.; Park, K. P.; Huh, D. G.; Lee, J.; Kim, S. J.; Lee, H. *Energy Fuels* **2008**, *22*, 3160.
- (10) Zhou, X. T.; Tao, X. H.; Liang, D. Q.; Fan, S. S. *Energy Explor. Exploit.* **2008**, *26*, 267.
- (11) Linga, P.; Haligva, C.; Nam, S. C.; Ripmeester, J. A.; Englezos, P. *Energy Fuels* **2009**, *23*, 5508.
- (12) Kumar, A.; Maini, B.; Bishnoi, P. R.; Clarke, M.; Zatsepina, O.; Srinivasan, S. J. *Petrol. Sci. Eng.* **2010**, *70*, 109.
- (13) Reagan, M. T.; Moridis, G. J. *Geophys. Res. Lett.* **2007**, *34*, L22709.
- (14) Etiope, G.; Milkov, A. V.; Derbyshire, E. *Global Planet Change* **2008**, *61*, 79.
- (15) Reagan, M. T.; Moridis, G. J. *J. Geophys. Res., Oceans* **2008**, *113*, C12023.
- (16) Krey, V.; Canadell, J. G.; Nakicenovic, N.; Abe, Y.; Andrleit, H.; Archer, D.; Grubler, A.; Hamilton, N. T. M.; Johnson, A.; Kostov, V.; Lamarque, J. F.; Langhorne, N.; Nisbet, E. G.; O'Neill, B.; Riahi, K.; Riedel, M.; Wang, W. H.; Yakushev, V. *Environ. Res. Lett.* **2009**, *4*, 034007.
- (17) Galloway, T. J.; Ruska, W.; Chappele, P.; Kobayash, R. *Ind. Eng. Chem. Fund.* **1970**, *9*, 237.
- (18) Deroo, J. L.; Peters, C. J.; Lichtenhaler, R. N.; Diepen, G. A. M. *AICHE J.* **1983**, *29*, 651.
- (19) Sum, A. K.; Burruss, R. C.; Sloan, E. D. *J. Phys. Chem. B* **1997**, *101*, 7371.
- (20) Seo, Y. T.; Kang, S. P.; Lee, H. *Fluid Phase Equilib.* **2001**, *189*, 99.
- (21) Ohmura, R.; Uchida, T.; Takeya, S.; Nagao, J.; Minagawa, H.; Ebinuma, T.; Narita, H. *J. Chem. Thermodyn.* **2003**, *35*, 2045.
- (22) Jager, M. D.; de Deugd, R. M.; Peters, C. J.; Arons, J. D.; Sloan, E. D. *Fluid Phase Equilib.* **1999**, *165*, 209.
- (23) Guo, T. M.; Qiu, J. H. *Abstr. Pap. Am. Chem. Soc.* **1997**, *213*, 38.
- (24) Freer, E. M.; Selim, M. S.; Sloan, E. D. *Fluid Phase Equilib.* **2001**, *185*, 65.
- (25) Qiu, J. H.; Guo, T. M. *Chin. J. Chem. Eng.* **2002**, *10*, 316.
- (26) Kashchiev, D.; Firoozabadi, A. J. *Cryst. Growth* **2003**, *250*, 499.
- (27) Cathles, L. M.; Chen, D. F. J. *Geophys. Res., Solid Earth* **2004**, *109*, B08102.
- (28) Lin, W.; Chen, G. J.; Sun, C. Y.; Guo, X. Q.; Wu, Z. K.; Liang, M. Y.; Chen, L. T.; Yang, L. Y. *Chem. Eng. Sci.* **2004**, *59*, 4449.
- (29) Moudrakovski, I. L.; McLaurin, G. E.; Ratcliffe, C. I.; Ripmeester, J. A. *J. Phys. Chem. B* **2004**, *108*, 17591.
- (30) Jeon, Y. H.; Kim, N. J.; Chun, W. G.; Lim, S. H.; Kim, C. B.; Hur, B. K. J. *Ind. Eng. Chem.* **2006**, *12*, 733.
- (31) Sun, X. F.; Mohanty, K. K. *Chem. Eng. Sci.* **2006**, *61*, 3476.
- (32) Gualdrón, D. A. G.; Balbuena, P. B. *J. Phys. Chem. C* **2007**, *111*, 15554.
- (33) Kowalsky, M. B.; Moridis, G. J. *Energy Convers. Manage.* **2007**, *48*, 1850.
- (34) Luo, Y. T.; Zhu, J. H.; Fan, S. S.; Chen, G. J. *Chem. Eng. Sci.* **2007**, *62*, 1000.
- (35) Makogon, Y. F.; Melikhov, I. V.; Kozlovskaya, E. D.; Bozhevol'nov, V. E. *Russ. J. Phys. Chem. A* **2007**, *81*, 1645.
- (36) Sun, C. Y.; Chen, G. J.; Ma, C. F.; Huang, Q.; Luo, H.; Li, Q. P. *J. Cryst. Growth* **2007**, *306*, 491.
- (37) Hashemi, S.; Macchi, A.; Servio, P. *Ind. Eng. Chem. Res.* **2009**, *48*, 6983.
- (38) Talaghat, M. R.; Esmaeilzadeh, F.; Fathiakjahi, J. *Fluid Phase Equilib.* **2009**, *279*, 28.
- (39) Di Profio, P.; Area, S.; Germani, R.; Savelli, G. *J. Fuel Cell Sci. Technol.* **2007**, *4*, 49.
- (40) Ganji, H.; Manteghian, M.; Mofiad, H. R. *Fuel Process. Technol.* **2007**, *88*, 891.
- (41) Kumar, R.; Linga, P.; Moudrakovski, I.; Ripmeester, J. A.; Englezos, P. *AICHE J.* **2008**, *54*, 2132.
- (42) Ogawa, H.; Imura, N.; Miyoshi, T.; Ohmura, R.; Mori, Y. H. *Energy Fuels* **2009**, *23*, 849.
- (43) Chialvo, A. A.; Houssa, M.; Cummings, P. T. *J. Phys. Chem. B* **2002**, *106*, 442.
- (44) English, N. J.; MacElroy, J. M. D. *J. Comput. Chem.* **2003**, *24*, 1569.
- (45) Chihaiia, V.; Adams, S.; Kuhs, W. F. *Chem. Phys.* **2005**, *317*, 208.
- (46) Moon, C.; Taylor, P. C.; Rodger, P. M. *J. Am. Chem. Soc.* **2003**, *125*, 4706.
- (47) Guo, G. J.; Zhang, Y. G.; Zhao, Y. J.; Refson, K.; Shan, G. H. *J. Chem. Phys.* **2004**, *121*, 1542.
- (48) Guo, G. J.; Zhang, Y. G.; Refson, K. *Chem. Phys. Lett.* **2005**, *413*, 415.
- (49) Guo, G. J.; Zhang, Y. G.; Liu, H. *J. Phys. Chem. C* **2007**, *111*, 2595.
- (50) Guo, G. J.; Zhang, Y. G.; Li, M.; Wu, C. H. *J. Chem. Phys.* **2008**, *128*, 194504.
- (51) Guo, G. J.; Li, M.; Zhang, Y. G.; Wu, C. H. *Phys. Chem. Chem. Phys.* **2009**, *11*, 10427.
- (52) Mastny, E. A.; Miller, C. A.; de Pablo, J. J. *J. Chem. Phys.* **2008**, *129*, 034701.
- (53) Hawtin, R. W.; Quigley, D.; Rodger, P. M. *Phys. Chem. Chem. Phys.* **2008**, *10*, 4853.
- (54) Walsh, M. R.; Koh, C. A.; Sloan, E. D.; Sum, A. K.; Wu, D. T. *Science* **2009**, *326*, 1095.
- (55) Nada, H. *J. Phys. Chem. B* **2006**, *110*, 16526.
- (56) Vatamanu, J.; Kusalik, P. G. *J. Phys. Chem. B* **2006**, *110*, 15896.
- (57) Vatamanu, J.; Kusalik, P. G. *J. Am. Chem. Soc.* **2006**, *128*, 15588.
- (58) Vatamanu, J.; Kusalik, P. G. *J. Phys. Chem. B* **2008**, *112*, 2399.
- (59) English, N. J.; MacElroy, J. M. D. *J. Chem. Phys.* **2004**, *120*, 10247.
- (60) English, N. J.; Johnson, J. K.; Taylor, C. E. *J. Chem. Phys.* **2005**, *123*, 244503.
- (61) English, N. J.; Phelan, G. M. *J. Chem. Phys.* **2009**, *131*, 074704.
- (62) Myshakin, E. M.; Jiang, H.; Warzinski, R. P.; Jordan, K. D. *J. Phys. Chem. A* **2009**, *113*, 1913.
- (63) Rodger, P. M.; Forester, T. R.; Smith, W. *Fluid Phase Equilib.* **1996**, *116*, 326.
- (64) Carver, T. J.; Drew, M. G. B.; Rodger, P. M. *J. Chem. Soc., Faraday Trans.* **1995**, *91*, 3449.
- (65) Carver, T. J.; Drew, M. G. B.; Rodger, P. M. *J. Chem. Soc., Faraday Trans.* **1996**, *92*, 5029.
- (66) Duffy, D. M.; Moon, C.; Rodger, P. M. *Mol. Phys.* **2004**, *102*, 203.
- (67) Hawtin, R. W.; Rodger, P. M. *J. Mater. Chem.* **2006**, *16*, 1934.
- (68) Moon, C.; Hawtin, R. W.; Rodger, P. M. *Faraday Discuss.* **2007**, *136*, 367.
- (69) Moon, C.; Taylor, P. C.; Rodger, P. M. *Can. J. Phys.* **2003**, *81*, 451.
- (70) San-Miguel, M. A.; Rodger, P. M. *J. Mol. Struct.: THEOCHEM* **2000**, *506*, 263.
- (71) Storr, M. T.; Rodger, P. M. *Gas Hydr.: Challenges Future* **2000**, *912*, 669.
- (72) Storr, M. T.; Taylor, P. C.; Monfort, J. P.; Rodger, P. M. *J. Am. Chem. Soc.* **2004**, *126*, 1569.
- (73) Kvamme, B.; Huseby, G.; Forrisdahl, O. K. *Mol. Phys.* **1997**, *90*, 979.
- (74) Anderson, B. J.; Tester, J. W.; Borghi, G. P.; Trout, B. L. *J. Am. Chem. Soc.* **2005**, *127*, 17852.
- (75) Kvamme, B.; Kuznetsova, T.; Aasoldsen, K. *Mol. Simul.* **2005**, *31*, 1083.
- (76) Bernal, J. D.; Fowler, R. H. *J. Chem. Phys.* **1933**, *1*, 515.
- (77) Cerius2; Molecular Simulations Inc.: San Diego, 1999.
- (78) Jorgensen, W. L.; Chandrasekhar, J.; Madura, J. D.; Impey, R. W.; Klein, M. L. *J. Chem. Phys.* **1983**, *79*, 926.
- (79) Jorgensen, W. L.; Maxwell, D. S.; TiradoRives, J. *J. Am. Chem. Soc.* **1996**, *118*, 11225.
- (80) Peters, B.; Zimmermann, N. E. R.; Beckham, G. T.; Tester, J. W.; Trout, B. L. *J. Am. Chem. Soc.* **2008**, *130*, 17342.
- (81) Ota, M.; Ferdows, M. *JSME Int. J., Ser. B* **2005**, *48*, 802.
- (82) Radhakrishnan, R.; Trout, B. L. *J. Chem. Phys.* **2002**, *117*, 1786.
- (83) Cao, Z. T.; Tester, J. W.; Sparks, K. A.; Trout, B. L. *J. Phys. Chem. B* **2001**, *105*, 10950.
- (84) Cao, Z. T.; Tester, J. W.; Trout, B. L. *J. Chem. Phys.* **2001**, *115*, 2550.

- (85) Steve, P.; Paul, C.; Aidan, T. *Large-Scale Atomic/Molecular Massively Parallel Simulator*; Sandia National Labs: Albuquerque, 2009.
- (86) Hoover, W. G. *Phys. Rev. A* **1985**, *31*, 1695.
- (87) Hoover, W. G. *Phys. Rev. A* **1986**, *34*, 2499.
- (88) Melchionna, S.; Ciccotti, G.; Holian, B. L. *Mol. Phys.* **1993**, *78*, 533.
- (89) Darden, T.; York, D.; Pedersen, L. *J. Chem. Phys.* **1993**, *98*, 10089.
- (90) Hockney, R. W.; Eastwood, J. W. *Computer Simulation Using Particles*; Adam Hilger: New York, 1989.
- (91) Pollock, E. L.; Glosli, J. *Comput. Phys. Commun.* **1996**, *95*, 93.
- (92) Fidler, J.; Rodger, P. M. *J. Phys. Chem. B* **1999**, *103*, 7695.
- (93) Baez, L. A.; Clancy, P. *Ann. N.Y. Acad. Sci.* **1994**, *715*, 177.
- (94) Abascal, J. L. F.; Sanz, E.; Fernandez, R. G.; Vega, C. *J. Chem. Phys.* **2005**, *122*, 234511.
- (95) Fernandez, R. G.; Abascal, J. L. F.; Vega, C. *J. Chem. Phys.* **2006**, *124*, 144506.
- (96) Abascal, J. L. F.; Vega, C. *Phys. Chem. Chem. Phys.* **2007**, *9*, 2775.
- (97) Rahman, A.; Stillinger, Fh. *J. Am. Chem. Soc.* **1973**, *95*, 7943.
- (98) Speedy, R. J.; Mezei, M. *J. Phys. Chem.* **1985**, *89*, 171.
- (99) Belch, A. C.; Rice, S. A. *J. Chem. Phys.* **1987**, *86*, 5676.
- (100) Speedy, R. J.; Madura, J. D.; Jorgensen, W. L. *J. Phys. Chem.* **1987**, *91*, 909.

JP102874S